Cross-linked cellulose nanocrystal aerogels as viable bone tissue scaffolds

Daniel A. Osorio [a,b], Bryan E.J. Lee [c], Jacek M. Kwiecien [d,e], Xiaoyue Wang [a], Iflah Shahid [a], Ariana L. Hurley [a], Emily D. Cranston [b,f,g,⇑], Kathryn Grandfield [a,c,⇑]

[a]Department of Material Science and Engineering, McMaster University, 1280 Main Street West, Hamilton, ON L8S 4L7, Canada
[b]Department of Chemical Engineering, McMaster University, 1280 Main Street West, Hamilton, ON L8S 4L7, Canada
[c] School of Biomedical Engineering, McMaster University, 1280 Main Street West, Hamilton, ON L8S 4L7, Canada
[d]Department of Pathology and Molecular Medicine, McMaster University, 1280 Main Street West, Hamilton, ON L8S 4L7, Canada
[e]Department of Clinical Pathomorphology, Medical University of Lublin, Aleje Raclawickie 1, Lublin, Poland
[f]Department of Wood Science, The University of British Columbia, 2424 Main Mall, Vancouver, BC V6T 1Z4, Canada
[g]Department of Chemical and Biological Engineering, The University of British Columbia, 2360 East Mall, Vancouver, BC V6T 1Z3, Canada

article info

Article history:
Received 31 October 2018
Received in revised form 21 January 2019 Accepted 24 January 2019
Available online 30 January 2019

Keywords:
Cellulose nanocrystal
Aerogel
Tissue scaffold
Bone regeneration
Biomaterials

abstract

Chemically cross-linked cellulose nanocrystal (CNC) aerogels possess many properties beneficial for bone tissue scaffolding applications. CNCs were extracted using sulfuric acid or phosphoric acid, to produce CNCs with sulfate and phosphate half-ester surface groups, respectively. Hydrazone cross-linked aerogels fabricated from the two types of CNCs were investigated using scanning electron microscopy, X-ray micro-computed tomography, X-ray photoelectron spectroscopy, nitrogen sorption isotherms, and compression testing. CNC aerogels were evaluated in vitro with osteoblast-like Saos-2 cells and showed an increase in cell metabolism up to 7 days while alkaline phosphatase assays revealed that cells maintained their phenotype. All aerogels demonstrated hydroxyapatite growth over 14 days while submerged in simulated body fluid solution with a 0.1 M $CaCl_2$ pre-treatment. Sulfated CNC aerogels slightly outperform phosphated CNC aerogels in terms of compressive strength and long-term stability in liquid environments, and were implanted into the calvarian bone of adult male Long Evans rats. Compared to controls at 3 and 12 week time points, sulfa ted CNC aerogels showed increased bone volume fraction of 33% and 50%, respectively, compared to controls, and evidence of osteoconductivity. These results demonstrate that cross-linked CNC aerogels are flexible, porous and effectively facilitate bone growth after they are implanted in bone defects.

Statement of Significance

Due to the potential complications associated with autografts, there is a need for synthetic bone tissue scaffolds. Here, we report a new naturally-based aerogel material for bone regeneration made solely from chemically cross-linked cellulose nanocrystals (CNC). These highly porous CNC aerogels were shown to promote the proliferation of bone-like cells and support the growth of hydroxyapatite on their surface in vitro. The first in vivo study on these materials was conducted in rats and showed their osteconductive properties and an increase in bone volume up to 50% compared to sham sites. This study demonstrates the potential of using functionalized cellulose nanocrystals as the basis for aerogel scaffolds for bone tissue engineering.

1. Introduction

As treatments for bone disorders and defects have increased in recent years due to the aging population, there is a growing need for the use of synthetic materials as effective scaffolds for bone tissue regeneration [1]. Tissue scaffolds are 3D structures meant to facilitate, and in some cases promote, tissue growth [2]. In recent years, tissue scaffolds have been made of several biomaterials, such as chitosan, alginate and silk, through several fabrication techniques, in order to produce an ideal scaffold [3]. While the ideal characteristics of a bone scaffold are still debated, there are some

key features that scaffolds should possess. Scaffolds should be highly porous to promote vascularization into the defect area, and pores should be sufficiently large to allow migration of osteo genic cells through the scaffold; an optimum value often considered is in the range of 100–350 mm in diameter [1,4]. Other desirable characteristics include tuneable bioresorbability (the ability to degrade at the appropriate rate within the host tissue), non-toxicity in both its bulk and degraded forms, and the presence of favourable surface topography and chemistry to promote protein adhesion and cell differentiation [5]. Many scaffolds and bone grafts possess these characteristics but have difficulty conforming to the shape of bone defects [6]. This can lead to vacancies between the scaffold and the defect wall which can lead to incomplete bone healing [7]. This has prompted the investigation of new shape conforming materials for bone tissue scaffolds.

Cellulose nanocrystals (CNCs) are rod-shaped crystalline nanoparticles that are isolated from natural cellulose through an acid hydrolysis procedure [8]. CNCs have proven to be popular in several biomedical systems including drug-delivery [9,10], antibacterial applications [11], and tissue engineering [12,13]. CNCs can be phosphorylated [14], which is useful as phosphorylation of other cellulose substrates (bacterial and nanofibrillar cellulose) can promote hydroxyapatite (HA) growth, an essential indicator for osteoconduction and bone growth [15–17]. Moreover, CNCs are non-cytotoxic [18] and have been shown to facilitate cell proliferation in CNC-polylactic acid composite scaffolds [12]. Unfortunately, previous scaffold-like materials made solely of CNCs disintegrate in aqueous environments because they are only held together with weak cellulose-cellulose bonds (e.g. hydrogen bonding and van der Waals forces) [19]. This has resulted in CNCs being preferred as additives in nanocomposite tissue scaffolds, as opposed to ‘‘CNC-only” materials, where their role is to either improve mechanical properties of the matrix or enhance cell adhesion [12,20]. In recent work, Huang et al. [21] showed that HA/CNC based scaffold, cross-linked with poly(methyl vinyl ether alt-maleic acid), have potential as bone tissue scaffolds through preliminary in vitro protein adhesion studies and simulated body fluid (SBF) testing.

Our group has demonstrated that the addition of aldehyde and hydrazide functional groups to CNC surfaces allows for the formation of hydrazone bonds when CNCs are brought into contact [22]. The formation and degradation of hydrazone cross-links has been shown to be suitable for biomedical applications [23], and allows for the formation of a chemically cross-linked CNC aerogel which retains its structure in aqueous environments and has shape recovery properties [22]. Considering that degradation products from hydrazone bonds and the CNCs themselves are non-toxic [18] we can infer that the possibility of leachates during degradation of the aerogels is unlikely. The sponge-like characteristics of these CNC aerogels [22] may also facilitate the impregnation of other biomolecules. The robust nature and high porosity of hydra zone cross-linked CNC aerogels has led to applications as energy storage devices for flexible electronics and as re-usable water purification devices [24,25].

To thoroughly examine the potential of CNC aerogels as bone tissue scaffolds, two types of CNC aerogels were prepared and evaluated. Specifically, the aerogels were produced using CNCs with different surface chemistry; either sulfate half-ester groups (S-CNCs), made through the conventional sulfuric acid hydrolysis procedure [26], or phosphate half-ester groups (P-CNCs), made through an optimized phosphoric acid hydrolysis procedure [27].

The morphological and mechanical properties of both types of CNC aerogels were characterized, and were tested through in vitro cellular assays and in vivo implantation to determine their potential effectiveness as a bone tissue scaffold.

2. Methods and materials

2.1. Materials

Whatman cotton ashless filter aid was purchased at GE Health care Canada (Mississauga, Canada). Dimethyl sulfoxide (DMSO), 95–98% sulfuric acid, and 85% phosphoric acid were purchased from Caledon Laboratory Chemicals (Georgetown, Canada). Anhy drous ethanol was purchased from Commercial Alcohols (Toronto, Canada). 2,2,6,6-(tetramethylpiperidin-1-yl)oxyl (TEMPO, 99% purified by sublimation), adipic acid dihydrazide (ADH) 98%, N^0-ethyl-N-(3-(dimethylamino)propyl)-carbodiimide (EDC, com mercial grade), ethylene glycol (99.8%), silver(I) oxide (Ag_2O, 99.99% trace metals basis), sodium periodate ($NaIO_4$, >99.8%), N-hydroxysuccinimide (NHS, 97%), sodium hypochlorite solution (NaClO, 10–15%), sodium bromide (NaBr, Reagent Plus 99%), thiocarbohydrazide (TCH) 98%, Trypsin-EDTA (0.25), penicillin/ streptomycin, triton X-100, and phosphate-buffered saline were purchased from Sigma-Aldrich (Oakville, Canada). Osmium tetrox ide solution was purchased from Canemco & Marivac (Lakefield, Canada). Hydrochloric acid (HCl, 0.1 M and 1 M) and sodium hydroxide (NaOH, 0.1 M and 1 M) were purchased from LabChem Inc (Zelienople, USA). The water used was purified type I water with a resistivity of 18.2 MX cm (Barnstead NANOpure Diamond system, ThermoScientific, Asheville, USA). AlamarBlue , McCoy’s modified 5A media, and Saos-2 cells (ATCC, Manassas, USA), and fetal bovine serum were purchased from Life Technologies Inc. (Carlsbad, USA). Alkaline phosphatase assay and Abcam buffer was purchased from Abcam (Cambridge, UK). No chemicals were modified or further purified before use.

2.2. Preparation of cellulose nanocrystals

Refer to Supplementary Information.

2.3. CNC degree of functionalization

Surface group content for sulfate half-ester [28], aldehyde [29], carboxylic acid, and hydrazide [22] groups (surface functionalization methods can be found in supplementary information) were quantified through conductometric titration. For each titration, 12–15 mg of dry CNCs were added to 60 mL of purified water, 0.3 mL of 200 mM NaCl was added before each titration to gain a measurable conductivity reading. For aldehyde CNCs (CHO-CNC), carboxylic CNCs (COOH-CNC) and hydrazide CNCs (NH_2NH-CNC) titrations, 0.3 mL of 1 M HCl was added to the titration solution prior to titrating to introduce a strong acid slope to properly measure carboxylic acid content [30]. Sulfate half-ester groups on S-CNCs were titrated using 0.250 mL aliquots of 2 mM NaOH. CHO-CNCs, COOH-CNCs and NH_2NH-CNCs were titrated using 0.05 mL aliquots of 10 mM NaOH. Since hydrazide groups are grafted to carboxylic acid groups, the carboxylic content remaining on NH_2NH-CNCs was subtracted from the carboxylic content on COOH-CNCs to quantify the number of hydrazide groups. Aldehyde groups on CHO-CNCs were measured by selectively oxidizing aldehyde groups into carboxylic acid groups with an Ag_2O oxidation reaction, as reported by Campbell et al. [29], where 0.193 g of Ag_2O and 0.027 g of dry NaOH were added to a 20 mL 0.25 wt% suspension of CHO-CNCs and allowed to stir overnight. The CHO-CNC suspension was then passed through a 1 mm pore size glass microfiber filter and titrated using 0.05 mL aliquots of 10 mM NaOH. Each titration was completed in a period of approximately 1 h

2.4. Colorimetric determination of phosphate groups on CNCs

Phosphate half-ester content was quantified through colorimetric determination with a Hach DR 2800 portable spectrophotometer (Hach, London, Canada) [27]. A PhosVer 3 Ascorbic Acid Powder Pillow from Hach was added to 10 mL of a 0.1 wt% suspension of P-CNCs. The mixture was shaken vigorously for 30 s and allowed to settle for 2 min. The molybdate in the powder pillows reacts with free phosphate groups to create phosphomolybdic complexes producing a blue color [31]. This color can be read through an absorbance reading at 880 nm to quantify phosphate content. To remove any possible background noise, a separate 10 mL 0.1 wt% suspension of P-CNC was prepared and used as a blank.

2.5. Aerogel processing

Both S-CNC and P-CNC aerogels were prepared through cryo templating [22]. A 2.5 mL 2 wt% CHO-CNC suspension was combined with a 2.5 mL 2 wt% NH_2NH-CNC suspension, 0.5 mL of 200 mM NaCl, and 4.5 mL of purified water to make a 1 wt% sus pension of CHO-CNC/NH_2NH-CNC. The CNC suspension was then vortexed with an Analog Vortex Mixer (VWR, Mississauga, Canada) for 2 min. Suspensions were transferred to 15 mm and 8 mm diameter shell vials, acting as aerogel moulds, in either 0.5 mL or 1 mL aliquots to produce samples for characterization. All suspensions (in their moulds) were then frozen at 4 C overnight to turn the suspension into a cryo-gel. The cryo-gels were then transferred into anhydrous ethanol, to solvent exchange ice-crystals for ethanol, for 5 days to form alco-gels. No collapse of cryo-gels was observed during the solvent exchange, thereby making incremental ethanol exchanges unnecessary. The alco-gels were placed inside of a critical point dryer and solvent exchanged with supercritical CO_2 and gradually depressurized to ambient conditions to produce a CNC aerogel. Critical point drying (CPD) was performed with a Leica EM CPD300 (Vienna, Austria).

2.6. Dynamic light scattering (DLS)

Relative apparent particle size for all CNCs was measured through DLS with a Malvern Zetasizer Nano particle analyzer (Malvern Instruments, Malvern, UK). The term ‘‘apparent” is used to describe particle size measurements for CNC due to CNC particles being rod-shaped and DLS assumes spherical particles [32]. Therefore we consider DLS a valid method for relative CNC characterization but recognize that it does not represent either CNC length or diameter. A 0.025 wt% CNC suspension with 10 mM NaCl was prepared and analyzed using DLS. All reported values were obtained over 11 measurements for three separate samples, with temperature maintained at 23 C during measurements. The standard deviation was calculated from three individual sample measurements.

2.7. Zeta potential

Zeta potential measurements for CNC samples were measured using a ZetaPlus electrophoretic mobility analyzer (Brookhaven Instruments Corp, Holtsville, USA). Zeta potential samples consisted of a 0.25 wt% CNC suspension with 10 mM NaCl; the NaCl addition is essential for obtaining accurate zeta potential measurements [33]. All zeta potential values are reported as an average of 10 measurements of 15 cycles each, at room temperature. Standard deviation was calculated from three individual sample measurements.

2.8. Brunauer-Emmett-Teller (BET) analysis of nitrogen sorption isotherms

Specific surface area and pore size distribution of both S-CNC and P-CNC aerogels were analyzed with Brunauer-Emmett-Teller (BET) analysis of nitrogen sorption isotherms using an autosorb iQ (Quantachrome, Boynton Beach, USA). Samples were first degassed, then kept under nitrogen gas for seven days at 100 C. Since CNCs are hydrophilic and CNC aerogels have large specific surface areas, extensive drying is required to remove any tightly bound water. Samples were then analyzed at 196 C with nitrogen gas adsorption and desorption probing. Pore size distribution analysis was calculated using the density functional theory (DFT) model. The DFT model was used to calculate average pore size because mesopores on the aerogel surfaces are non-uniform. The DFT model compensates for non-uniformity by not assuming nitrogen gas condenses as a half sphere meniscus, rather than the Barrett-Joyner-Halenda (BJH) analysis that does assume a half sphere meniscus [34]. Only isotherms showing no retention of water were used to calculate specific surface area.

2.9. Density calculation

The densities of all aerogels were calculated by dividing the mass of an aerogel by its apparent volume. The volume of each aerogel was calculated by taking diameter and height measurements of each aerogel with a digital calliper. The volume was calculated assuming the aerogel was a perfect cylinder. The mass of each aerogel was measured with an analytical balance (Mettler Toledo Inc., Mississauga, Canada, readability of 0.0001 g). The density values reported are an average of three separate samples for each type of CNC aerogel.

2.10. Surgical implantation

The Animal Ethics Research Board at McMaster University, following the Guidelines and Regulations by the Canadian Council of Animal Care approved the animal use protocol for this work (AUP 14-12-54). In this protocol CNC aerogel were implanted in 22 of 32 (total population tested n = 32), 16 week old (390–430 g) Long Evans rats.

For CNC aerogel implantation surgeries, rats were induced in 5% isoflurane in 95% oxygen and maintained in 4% isoflurane throughout the surgical procedure. The skin on the top of the head and neck was carefully shaved and disinfected with 70% alcohol and with iodine povidone before cut over the midline of the skull and the neck. After gently scraping of the periosteum and drying of the surface of the skull with cotton swabs soaked in 3% peroxide, a 2 mm diameter bone defect was drilled 1–2 mm caudal to bregma and 1–2 mm lateral to the midline with a drill bit equipped with a plastic sleeve limiting the depth of the drill to approximately 1.5 mm. The blood in the bone defect was blotted out and a 2 mm 1.5 mm CNC aerogel was placed in the bone defect. For the controls, the bone defect there was no CNC aerogel implanted. The skin was closed with stainless steel staples and rats were given a subcutaneous injection of 0.4 mL of ketoprofen (10 mg/ml, Ana fen, Merial Canada, Inc., Baie d'Urfe, Quebec, Canada), administered subcutaneously for analgesia for pain and also subcutaneous injection of 5 mL of saline before waking up from anaesthesia. Single ketoprofen injections were repeated for 2 more days post surgery.

Post-surgical implantations, analgesic treatment with ketoprofen was repeated once daily for two days after surgery, where the staples were removed 14 days post-surgery. Rats were monitored daily for the duration of the study for: swelling of the surgical wound, dehydration, lethargy, and the body weight was measured twice per week.
Rats were euthanized at 3 week and 12 week time points post surgery. For post-surgery analysis rats were randomly selected to be used for histology analysis (n = 12) and mCT analysis (n = 20). After the rats were euthanized, the calvarian bone of the skull, including the lesion were collected as follows: First histological analysis, the rats were overdosed with 80 mg sodium pentobarbital (Ceva, France) intraperitoneal to achieve a deep plane of anaesthesia at which time the thorax was opened and 100 IU heparin injected into the left ventricle. A cannula with tubing attached to the flowing lactated Ringer's solution was inserted into the left ventricle and the right auricle was cut to allow for the outflow of blood. After the washout of blood, the flow was switched to that of the phosphate buffered formalin for 8 min. The formalin-fixed carcass was placed in a closed container and refrigerated for 2– 3 h after which the calvarian bone was carefully cut out with small bone cutters from the skull and placed in formalin for 1 day. To soften the bone for histological analysis, the calvarian bone with the surgical lesion was then placed in a decalcifying solution; for malin supplemented with 4% EDTA, pH 7.2, and placed on a rotating shaker. The decalcifying solution was replaced twice a week and the bone became soft after 8–9 weeks when it was trimmed by cutting perpendicularly to the skull midline through the hole, processed in a rising concentration of ethyl alcohol and in xylene and embedded in paraffin wax, cut at 5 lm thick sections and being immersed in a 5% Alcian blue solution for pre-staining before OTO staining.

Acquisition and post-processing: All mCT was performed using a Skyscan 1172 (Bruker, Massachusetts, USA) with a 40 kV X-ray beam, with no filter. In vitro samples were evaluated with a cubic voxel size of 5 mm and 0.3 rotation step, whereas in vivo samples were evaluated with a cubic voxel size of 3.67 mm and 0.1 rotation step. The software package NRecon (Bruker, Massachusetts, USA) was used to reconstruct radiographs into a three-dimensional (3D) volume for further visualization in Avizo (FEI Company, Eindhoven, The Netherlands). For in vivo samples the dynamic image range was calculated to remove all noise and traces of aerogel. Additionally, a beam hardening correction of 75% and maximum ring artifact reduction were applied, as not to skew segmentation analysis.

Porosity measurements for both CNC aerogels were then performed by CTAn 1.16 software (Bruker, Billerica, USA). Porosity for CNC aerogels was also calculated using the following equation [22]. Where P(%) is the porosity of the aerogel, q_{Gel} is the density of the aerogel, and q_{CNC} is the density of CNCs, assumed to be 1.59 g/ cm^3 [37].

$$P(\%) = 100 * (1 - \frac{\rho_{Gel}}{\rho_{CNC}})$$

2.11. X-ray micro computed tomography (mCT)

Staining: The contrast of aerogel samples for mCT analysis was enhanced by using sequential osmium tetroxide/thiocarbohy drazide (TCH) staining or OTO staining [35]. Aerogel samples from SBF testing were prepared using 8 mm diameter shell vials as a mould with 0.5 mL of sample. Aerogels were submerged in 1 wt% osmium tetroxide solution for 1 h, and rinsed multiple times with purified water to remove osmium tetroxide. To ensure all osmium tetroxide had been removed from the aerogel, small aliquots of the rinsing solution were tested with a drop of 0.5 wt% solution of TCH. The aerogel was rinsed again if the solution changed colour. After the aerogel had been rinsed, the aerogel was submerged into a 0.5 wt% TCH solution for 15 min, followed by rinsing using the same procedure and criteria as previously mentioned, instead using a drop of 1 wt% osmium tetroxide as the indicator. After the aerogel was thoroughly rinsed, it was again submerged in a 1 wt% osmium tetroxide solution for 15 min, fully rinsed, followed by dehydration with a graded series of ethanol (25%, 50%, 70%, 70%, 95%, 95%, 100%, for 1 day each), and subjected to CPD.

Samples extracted from in vivo experiments (surgical implantation and extraction methods can be found in supplementary infor mation) were also subjected to Alcian Blue staining [36], prior to OTO staining as above. Briefly, harvested skulls were immersed in a solution of 4% glutaraldehyde in sodium cacodylate (pH 7) before being placed on a rocking table for 48 h at room temperature to allow for tissue fixation. Samples were subsequently washed three times on a rocking table with deionized water before

Segmentation of the reconstructed volumes of in vivo samples was completed in Avizo for FEI Systems 9.2.0 software (FEI Company, Eindhoven, The Netherlands). The volume of the total implant site was selected by tracing a 2 mm diameter circle over the bone defect of the reconstructed rat skull. Any fibrous tissue above the bone defector muscle tissue below the bone defect was not included in the segmentation. The total volume was calculated, then all empty space was removed using thresholding to determine the volume of bone present. As shown in Eq. (2), the bone volume fraction (BV/TV) was calculated by dividing bone volume (BV) by total volume (TV) and multiplied by 100% to represent as a percentage.

2.12. Bone volume fraction measurements

Segmentation of the reconstructed volumes of *in vivo* samples was completed in Avizo for FEI Systems 9.2.0 software (FEI Company, Eindhoven, The Netherlands). The volume of the total implant site was selected by tracing a 2 mm diameter circle over the bone defect of the reconstructed rat skull. Any fibrous tissue above the bone defector muscle tissue below the bone defect was not included in the segmentation. The total volume was calculated, then all empty space was removed using thresholding to determine the volume of bone present. As shown in Eq. (2), the bone volume fraction (*BV/TV*) was calculated by dividing bone volume (*BV*) by total volume (*TV*) and multiplied by 100% to represent as a percentage.

$$B_{volume\ fraction} = \frac{BV}{TV} * 100\%$$

2.13. Scanning electron microscopy (SEM) imaging

Sample preparation for SEM consisted of submerging aerogels into liquid nitrogen, freeze-fracturing to expose a cross-section, and mounting on a 1^{00} stainless steel stub with nickel paint, and sputter coating with 5 nm of platinum (aerogels only) or carbon (aerogels with SBF coatings). The sides of the aerogel were also coated with nickel paint to avoid charging while imaging. All images were taken using a JEOL 7000F SEM (JEOL, Tokyo, Japan) with an acceleration voltage of 2 kV. SEM sample preparation for aerogels with seeded cells consisted of fixation in 0.25% glutaraldehyde in a sodium cacodylate buffer for 1 day, followed by dehydration with a graded series of ethanol (25%, 50%, 70%, 70%, 95%, 95%, 100%, for 1 day each), before being stained with the osmium tetroxide/thiocarbohydrazide (TCH) staining protocol [35] and being coated with 5 nm of platinum coating. Samples with seeded cells were imaged with an acceleration voltage of 10 kV.

2.14. X-ray diffraction (XRD) analysis

Verification of HA was determined through XRD analysis using a Bruker 3-circle D8 goniometer and a Bruker Smart6000 CCD area detector (Bruker, Massachusetts, USA) with Cu Ka radiation. Raw CNC samples were prepared by freeze-drying CNC suspensions, then compressing a small portion of dried CNCs into a thin disk, to provide background spectra to monitor HA growth. CNC aerogels with HA coatings were prepared by drying CNC aerogels in an oven at 37 C overnight, then compressed into a thin disk. Frames were integrated in DIFFRAC.EVA (Bruker AXS, Version 4.0, Massachusetts, USA) and phase ID was performed using integrated database PDF-4+ 2016 [38]

2.15. X-ray photoelectron spectroscopy (XPS) analysis

A quantitative comparison of the hydrazone cross-link density between S-CNC and P-CNC aerogels was measured using XPS. Samples for XPS were prepared by freeze-drying CNC suspensions, a small portion of dried CNCs were then compressed into a thin disk. Samples were measured using a Physical Electronics (PHI) Quan tera II spectrometer (Chanhassen, USA) using an Al Ka X-ray source (1486.7 eV) operating at 50 W and 15 kV with a system pressure not allowed to exceed 1.0 10^{9} Torr and an operating pressure of 2.0 10^{8} Torr. Pass energy of 280 eV was used to collect the survey spectra and a 55 eV was used to collect high resolution nitrogen spectra. All spectra were collected at a take off angle of 45 and a dual beam charge compensation system was used for the neutralization of all samples. Data were processed using PHI MultiPak Version 9.4.0.7 software. The high-resolution nitrogen spectra was deconstructed into two primary nitrogen peaks, where the N1 peak is a combination of amine bonds (N H_2, Bond Energy = 399.88 eV) and hydrazine bonds (N-N), and the N2 peak are hydrazone bonds (C@N, Bond Energy = 401.41 eV). We consider the spectra to have an error as high as 5%.

2.16. Compression testing

Compressive strength of both S-CNC and P-CNC aerogels were measured using a Mach-1 Mechanical Testing System (Biomomen tum, Laval, Canada). Aerogels for mechanical testing were prepared in a 15 mm diameter shell vial as a mould with 1 mL of sample per aerogel so that all aerogels were the same diameter and height. All aerogels were compressed to 90% of their maximum height at a compression speed of 0.1 mm/s in both dry and aqueous conditions. In water, cyclic measurements were conducted, with the third cycle reported as the true compressive strength in wet conditions [39].

2.17. Cell culture

Saos-2, osteosarcoma, cells were grown and cultured as described in previous work [40]. Aerogel samples for all cell work were prepared using 15 mm diameter shell vials as a mould with 0.5 mL of sample. Aerogel samples were placed in a 24-well plate with 0.75 mL of media to fully submerge the aerogel sample. Cells were seeded at a density of 10,000 cells/cm^2 on each aerogel and allowed to incubate for 1, 3, and 7 days. It should be noted that since aerogels are opaque and strongly retain water-based fluids, wells with aerogels without any seeded cells were used as blanks.

2.18. Cell metabolism

Cell metabolism on aerogel surfaces was measured using an AlamarBlue assay using methods described previously [40]. AlamarBlue is a trademark for the compound resazurin which is irreversibly reduced to resorfin upon being introduced into the electrochemical half-reactions of the electron transport chain during cell metabolism. After incubation, the fluorescence of the aerogel samples was measured using an Infinite M200 Tecan (Männedorf, Switzerland) microplate reader with a 540 nm excitation wavelength and 580 nm emission. Aerogel samples were then washed with PBS to remove excess Alamarblue solution from the aerogel. After rinsing, 0.1% Triton X-100 in PBS solution was added to lyse cells for alkaline phosphatase activity analysis. All recorded values are the average and standard error of six individual samples per incubation time point.

2.19. Alkaline phosphatase activity

ALP activity is an early marker of osteoblast differentiation, indicating the formation of osteoblast matrix mineralization. A 0.05 mL aliquot was taken from the cell lysis solution and mixed with 0.1 mL of p-nitrophenol phosphate in Abcam buffer and allowed to incubate for 20 min. After incubation, absorbance readings of the aerogel samples were measured with an Infinite M200 Tecan (Männedorf, Switzerland) microplate reader at an emission wavelength of 405 nm. All recorded values are the average and standard error of six individual samples per incubation time point.

2.20. Statistical analysis on in vitro and in vivo tests

Statistical analysis was performed using the programming language, R (R Core Team, New Zealand), using two-way ANOVA at a significance level of a = 0.05 and Tukey's honest significant difference test was used to evaluate contrasts. All data from in vitro and in vivo experiments were accepted to be normally distributed as per the Shapiro-Wilk test (p >

0.05).

2.21. Simulated body fluid test

SBF was prepared according to the procedure outlined by Kokubo and Takadama [41]. Aerogel samples for SBF testing were prepared using 8 mm diameter shell vials as a mould with 0.5 mL of sample. Half of the S-CNC and P-CNC aerogel samples were pre-treated by submerging aerogels in 5 mL of 0.1 M $CaCl_2$ for 3 days at 37 C with 5% CO_2. This was to ensure calcium cations would ionically bond to free anionic groups on aerogel surfaces [42]. The other half of S-CNC and P-CNC aerogel sample size was not pre-treated, to see if the $CaCl_2$ rinse was essential for growing HA. Aerogel samples were submerged in 3 mL of SBF solution at 37 C, with 5% CO_2, for 7 and 14 day incubation periods, and the SBF solution was changed every 3–4 days. After incubation, samples were thoroughly washed with purified water and allowed to dry at 37 C overnight.

3. Results

3.1. CNC characterization

CNCs prepared by sulfuric acid and phosphoric acid hydrolysis were both functionalized to have orthogonal cross-linkable groups on their surface, i.e., aldehyde and hydrazide groups. The surface content and apparent particle size of all CNCs used in this work are shown in Table 1. On average, P-CNCs are larger than S-CNCs and the aldehyde surface modification on both types of CNCs tends to increase their particle size [43]. However, the aldehyde and hydrazide surface densities for both S-CNCs and P-CNCs are similar. This was done purposely so that S-CNC and P-CNC aerogels could theoretically form the same number of hydrazone cross links and produce as similar aerogels as possible.

Table 1. Surface content and apparent particle size for S-CNCs and P-CNCs before and after grafting with aldehyde and hydrazide groups. Zeta potential is only provided for S-CNCs. (CHO, COOH-, and NH2NH-, prefixes pertain to aldehyde, carboxylic acid, and hydrazide surface groups, respectively.))

Type of CNC	Sulfate Half-Ester Content (mmol/g)	Phosphate Half-Ester Content (mmol/g)	Aldehyde Content (mmol/g)	Carboxylic Acid Content (mmol/g)	Hydrazide Content (mmol/g)	Apparent Particle Size (nm)	Zeta Potential (mV)
S-CNC	0.212 ± 0.002	–	–	–	–	85 ± 1	−41 ± 3
CHO-S-CNC	0.198 ± 0.001	–	0.60 ± 0.05	–	–	140.1 ± 0.6	−21.1 ± 0.2
COOH-S-CNC	0.210 ± 0.002	–	–	1.20 ± 0.03	–	90.4 ± 0.6	−41 ± 5
NH2NH-S-CNC	0.211 ± 0.004	–	–	0.59 ± 0.03	0.63 ± 0.03	98.2 ± 0.8	−26 ± 2
P-CNC	–	0.051 ± 0.003	–	–	–	200 ± 2	–
CHO-P-CNC	–	0.022 ± 0.004	0.58 ± 0.05	–	–	308 ± 6	–

COOH-P-CNC	–	0.055 ± 0.005	–	1.02 ± 0.05	–	83.2 ± 0.2	–
NH2NH-P-CNC	–	0.052 ± 0.007	–	0.50 ± 0.01	0.53 ± 0.03	84 ± 1	–

As shown in Table 1, and mentioned above, the P-CNC particle size is larger than the S-CNC particle size. Two factors contribute to this, (1) the hydrolysis to produce P-CNCs is less harsh and larger particles are isolated [27] and (2) there are fewer grafted (and deprotonated) weak acid surface charge groups (phosphate half-esters) that are responsible for colloidal stability, thus we expect that minor CNC aggregation is occurring. Similarly, any surface modification that decreases the surface charge density (i.e., aldehyde/hydrazide) leads to slightly larger CNCs, again from CNC aggregation/association, whereas adding more surface charge (i.e., TEMPO oxidation) decreases the apparent particle size. This is mirrored in the zeta potential measurements for the S-CNCs; similar measurements for P-CNCs indicated low surface charge and a colloidally unstable system making zeta potential measurements unreliable for those samples. The size, degree of aggregation and colloidal stability of CNCs can influence how they assemble during aerogel fabrication, which in turn changes the behaviour and mechanical properties of CNC aerogels, and affects their tissue scaffolding potential, as discussed further below.

3.2. Aerogel characterization

Morphology for both types of aerogels was evaluated through SEM and mCT imaging. Fig. 1 shows that both types of aerogels con
sist of condensed CNC sheets (or flakes) separated by large macro pores, predominantly larger than 100 mm in diameter. Both S-CNC and P-CNC aerogels have similar sheet morphology and size. At higher magnification (insets in Fig. 1a and b), both types of aerogel sheets exhibit similar mesopore sizes. This is consistent with the bimodal pore morphology reported by Yang and Cranston [22]. BET isotherm analysis using the DFT model indicated the average mesopore size for S-CNC aerogels is 6 nm and for P-CNC aerogels is 11 nm. The specific surface area was measured to be 190 m^2/g and 130 m^2/g for S-CNC and P-CNC aerogels, respectively. The macropore morphology for both aerogels was similar by SEM image analysis in Fig. 1, and this was reinforced through the 3D mCT reconstructions shown in Fig. 2.

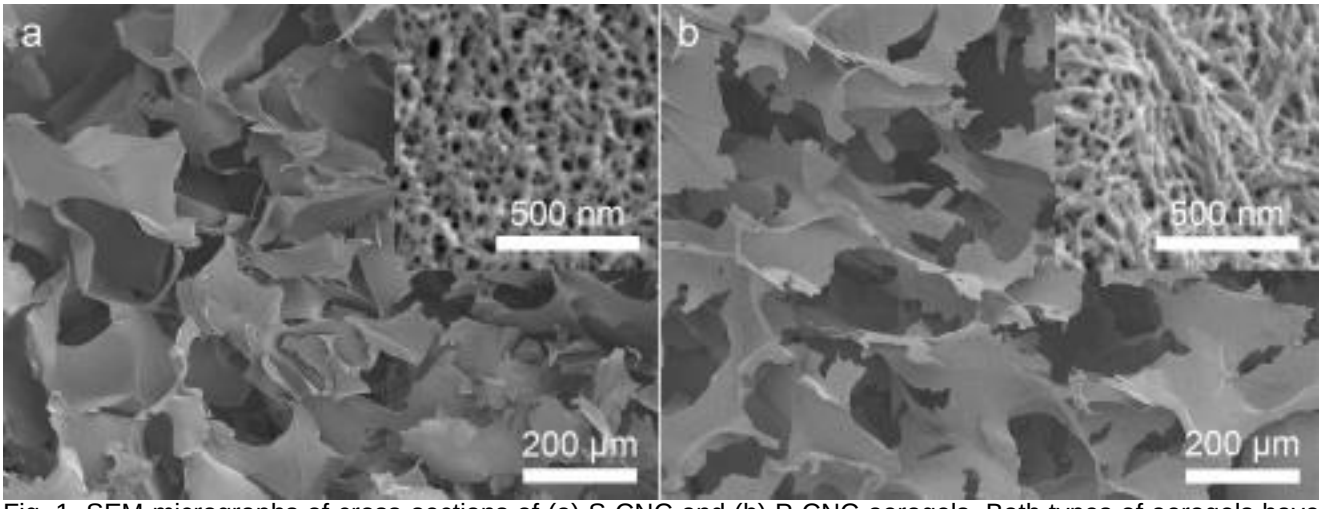

Fig. 1. SEM micrographs of cross-sections of (a) S-CNC and (b) P-CNC aerogels. Both types of aerogels have similar morphology with cross-linked CNC sheets (or flakes) separated by macropores. Insets at higher magnification show the similar mesoporous structures of the CNC sheets.

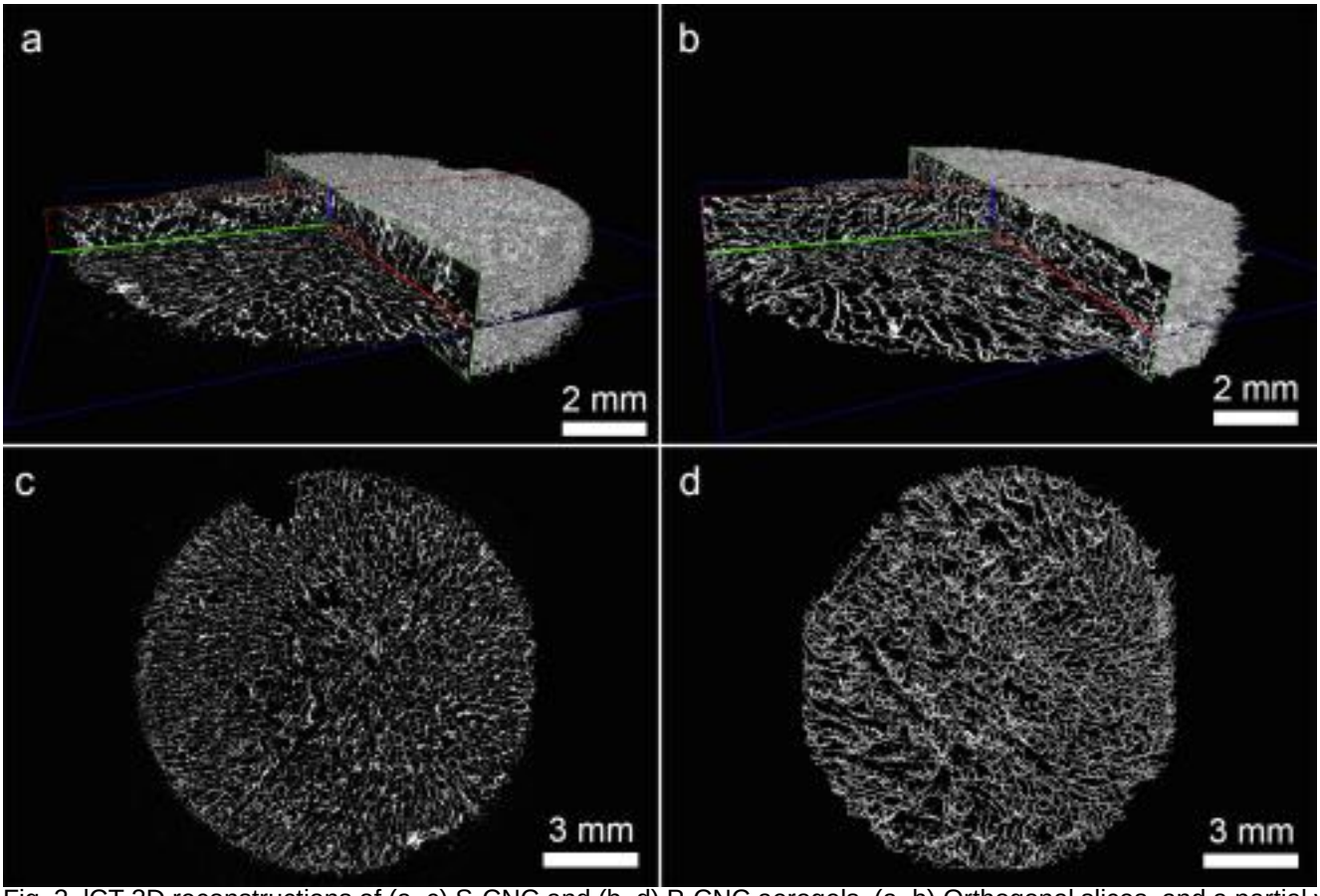

Fig. 2. lCT 3D reconstructions of (a, c) S-CNC and (b, d) P-CNC aerogels. (a–b) Orthogonal slices, and a partial volume rendering showing the interconnected pore structure and macropores ranging from 5 lm and larger. (c, d) The macroporous structure through a 2D xy slice through the center of the aerogels. 158 D.A. Osorio et al. / Acta Biomaterialia 87 (2019) 152–165

While S-CNC and P-CNC aerogels shared morphological similarities, their mechanical behaviour had notable differences. For example, cyclic mechanical testing in wet conditions indicated that P-CNC aerogels have the same flexibility and shape-recovery properties as shown previously for S-CNC aerogels [22]. However, compression data showed that S-CNC aerogels exhibited higher compressive strength at 90% compression than P-CNC aerogels in both dry and wet conditions (Fig. 3). For both types of aerogels, the materials were more easily compressed in water than in air, due to the plasticising effect of water.

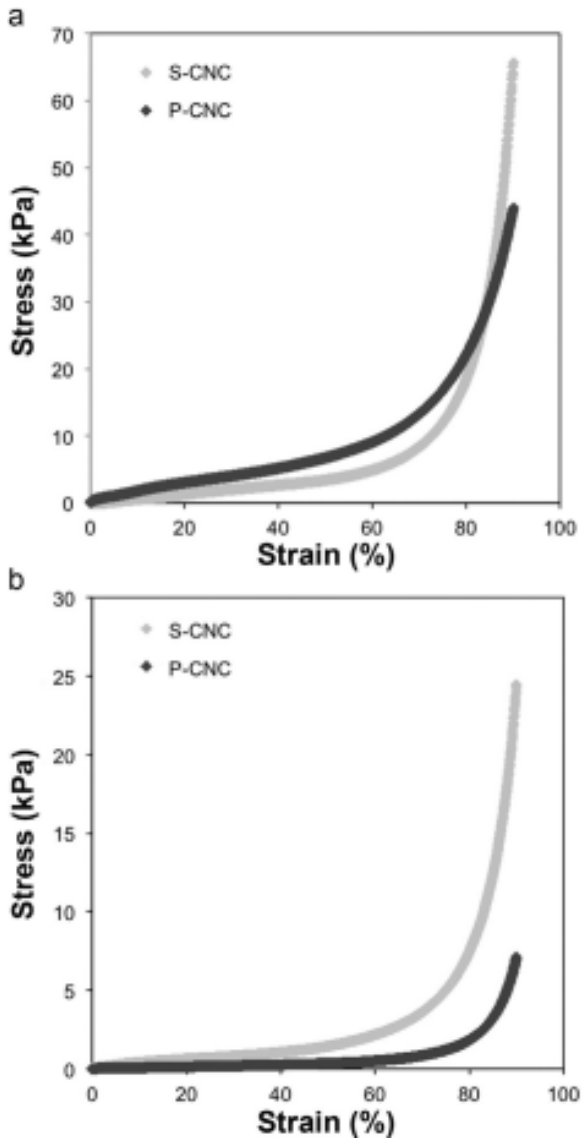

Fig. 3. Compressive stress-strain curves for S-CNC (grey) and P-CNC (black) aerogels from 0% to 90% strain in (a) dry conditions, (b) wet conditions, showing that S-CNC aerogels are more resistant to compression than P-CNC aerogels in both dry and wet conditions.

Chemical and physical differences between S-CNC and P-CNC aerogels were also quantified; from high resolution nitrogen spectra measured by XPS, S-CNC aerogels show a larger hydrazone peak, revealing three times more hydrazone bonds, as shown in Table 2. Density calculations indicated that S-CNC aerogels have a lower density, 10 ± 1 mg/cm^3, than P-CNC aerogels, 19 ± 2 mg/cm^3. Calculated porosity from density values indicate S-CNC aerogels have a porosity of 99.3%, while P-CNC aerogels have a porosity of 98.8%. This is reinforced through the porosity measurements made from 3D mCT reconstructions, where S-CNC aerogels have a porosity of 89.7% and P-CNC aerogels having a porosity of 83.9% (Fig. 2). The differences between the two sets of porosity calculations are due to the resolution limitation of μCT imaging. The analyzed radiographs cannot account for pores <5 μm, and therefore cannot resolve mesopores for either aerogel type. The difference between the two porosity calculations is attributed to the porosity provided by the mesopores on CNC sheets elucidating that 10–15% of the aerogel porosity comes from space between individual cross-linked CNCs.

Table 2. High-resolution nitrogen XPS spectra values for CNC aerogels.

	Atomic composition (%)

Type of aerogel	Amine/Hydrazine	Hydrazone
S-CNC	90.1	9.9
P-CNC	96.6	3.4

3.3. Aerogel cell testing

Cell proliferation and metabolism of Saos-2 cells on S-CNC and P-CNC sheets was performed at time points of 1, 3, and 7 days. The cell proliferation after 3 days on S-CNCs is shown in Fig. 4a and 4b. These images demonstrate characteristics of healthy cell adhesion, as the visible Saos-2 cells are oblong and elongated (Fig. 4a), with Fig. 4b showing filopodia extending over the CNC aerogel surface [44]. Cell metabolism on S-CNC aerogels increased between 1 and 3 days while maintaining the same level of cell metabolism between 3 and 7 days (Fig. 4c). P-CNC aerogels (although not shown in SEM images) also showed an increase in cell metabolism over 1, 3, and 7 days (Fig. 4c). While the metabolism was lower in P-CNC compared to S-CNC aerogels at 1 and 3 time points, by 7 days the amount of cell metabolism between the groups was comparable. At 3 days, there was a significant difference ($p < 0.05$) in metabolism between the aerogels but by 7 days this effect disappeared. The ALP activity for S-CNC aerogels showed a similar trend to the S-CNC aerogel cell metabolism (Fig. 4d). An increase in ALP activity was noted from 1 to 3 days, with the ALP activity staying statistically the same between 3 and 7 days. While a similar increase in ALP activity occurred between 1 and 3 days for P-CNC aerogels, a sharp increase in ALP activity occurred between 3 and 7 days. A statistically significant difference in ALP activity ($p < 0.05$) at 7 days is noted between the two aerogels.

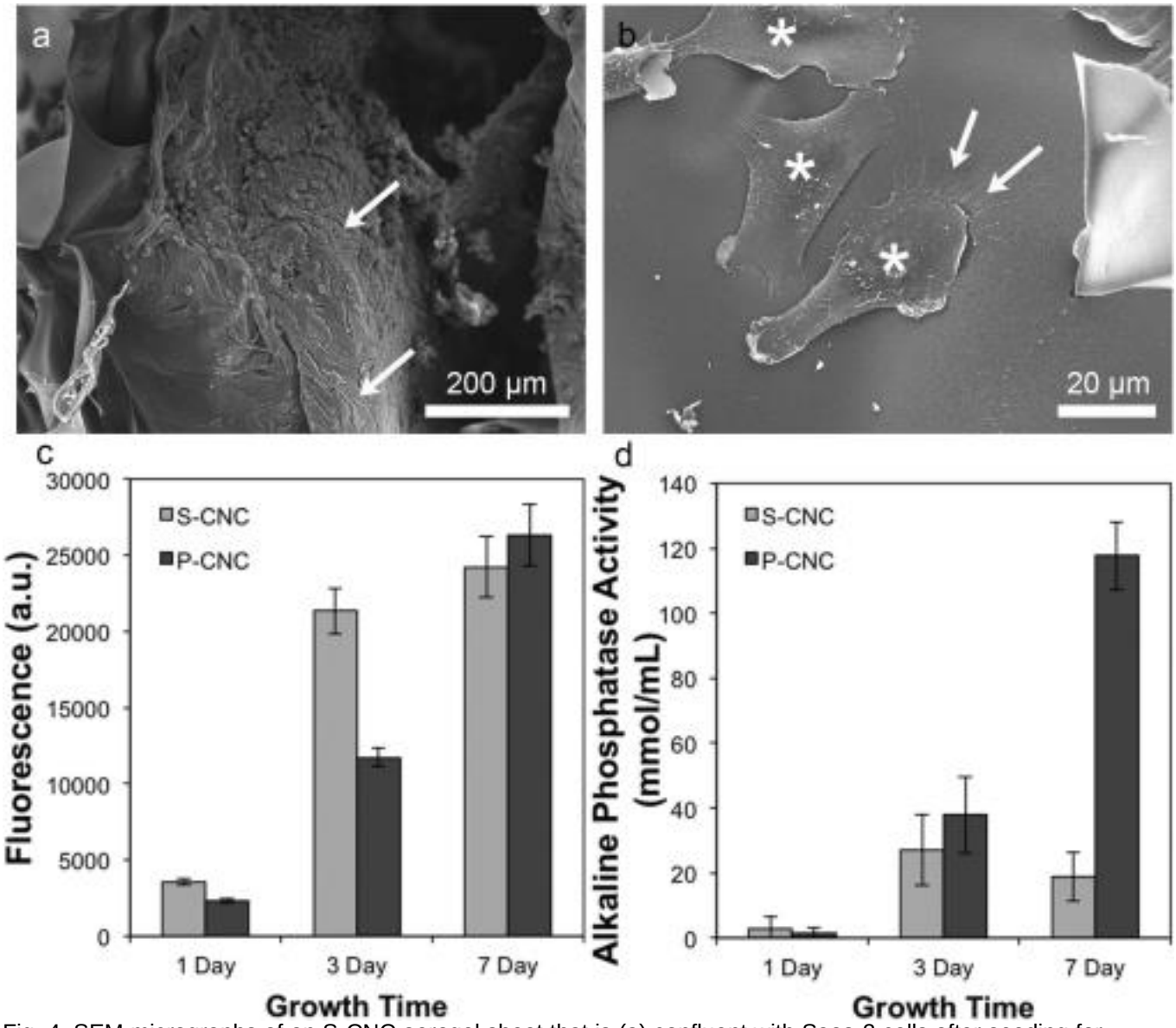

Fig. 4. SEM micrographs of an S-CNC aerogel sheet that is (a) confluent with Saos-2 cells after seeding for 3 days, marked by arrows, and (b) at higher magnification has distinct cells, marked by *, that show healthy characteristics, such as oblong shape and extending filopodia, marked by arrows. (c) Cell metabolism, and (d) alkaline phosphatase activity results comparing S-CNC and P-CNC aerogels for 1, 3, and 7 days.
160

3.4. Simulated body fluid testing

SEM images of S-CNC and P-CNC aerogels after 7 and 14 days in SBF are shown in Fig. 5. Both S-CNC and P-CNC aerogels nucleated HA, which is apparent by the flaky spherical structures (Fig. 5b and d)

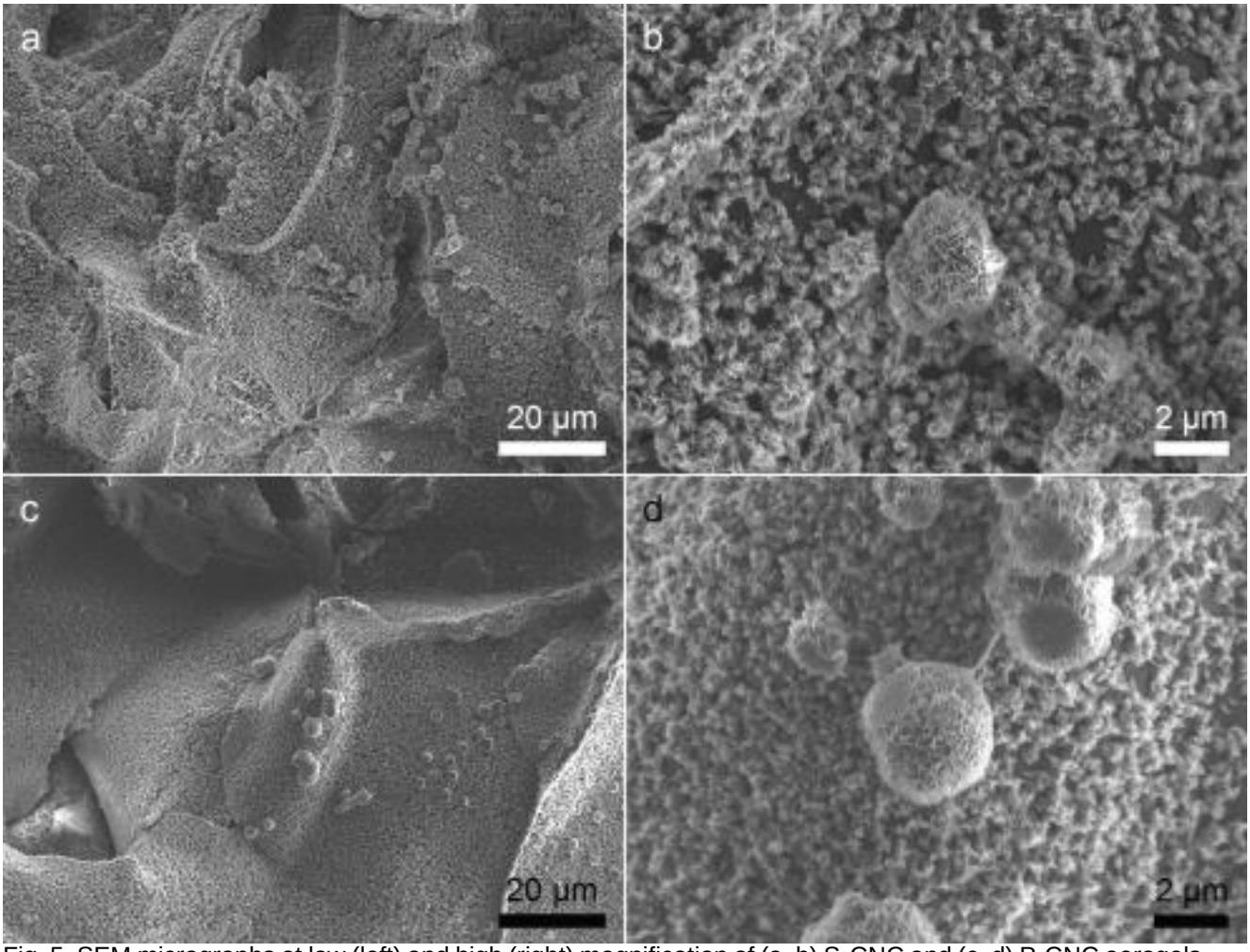

Fig. 5. SEM micrographs at low (left) and high (right) magnification of (a, b) S-CNC and (c, d) P-CNC aerogels after pre-treatment with calcium chloride and SBF submersion for 7 days. Characteristic flake-like HA crystals covered the surface of both types of aerogels, and contained Ca and P (EDX results not shown).

It should be noted that aerogel samples not subjected to a $CaCl_2$ pre-treatment did not grow HA. While preliminary electron dispersion x-ray spectroscopy (EDX) during SEM measurements indicated particles contained Ca and P ratios close to the stoichiometric ratio of HA, XRD analysis, Fig. 6, supports that the crystals shown in the SEM images are HA, and provides evidence for an increase in HA growth between 7 and 14 days through a sharpening and increase in peak intensity of characteristic HA peaks.

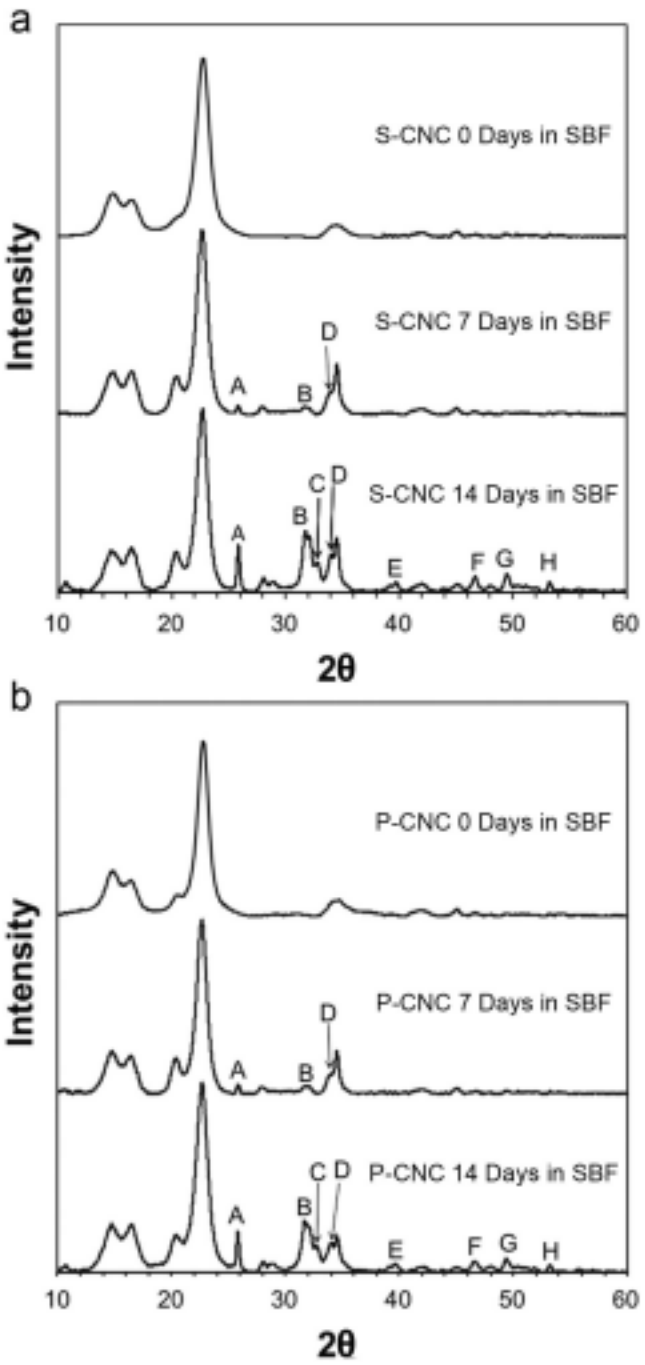

Fig. 6. XRD spectra for (a) S-CNC and (b) P-CNC aerogels at 0, 7, and 14 days. At 7 days, both types of aerogels show preliminary HA peaks forming. As submersion time in SBF increases to 14 days, peaks become more defined indicating an increase in the HA layer on CNC sheets. Characteristic HA peaks are marked A = 25.9 (0 0 2), B = 31.8 (2 1 1), C = 32.9 (3 0 0), D = 34.0 (2 0 2), E = 39.8 (3 1 0), F = 46.7 (2 2 2), G = 49.5 (2 1 3), and H = 53.2 (0 0 4) [38].

3.5. In vivo results

While the observed in vitro results between S- and P-CNC aero gels were comparable, S-CNC aerogels demonstrated stronger mechanical properties and higher amount of cross-linking groups. It was hypothesized that these properties would result in lower degradation rates, which would improve the long-term stability of the scaffold in vivo. Therefore, in vivo experiments in this study were limited to S-CNC aerogels. The histological analysis of S-CNC aerogels post-

implantation, shown in Fig. 7, revealed that in con trol rats at the 3 week time point, there was robust formation of new bone by distance osteogenesis from the edges of the bone defect only (Fig. 7a). This is supported by the observation of rows of hypertrophied osteoblasts on the surface of the new bone (Fig. 7b). However, in rats implanted with the S-CNC aerogel, bone formation was also observed in multiple areas within the center of the defect site. The implanted material (Fig. 7e) has apparently been internalized by large round cells with abundant ground material in the cytoplasm, adherent to each other and interpreted as macrophages (Fig. 7f). The new bone formation within the S-CNC aerogel is also supported by the identification of rows of hypertrophied osteoblasts (Fig. 7f).

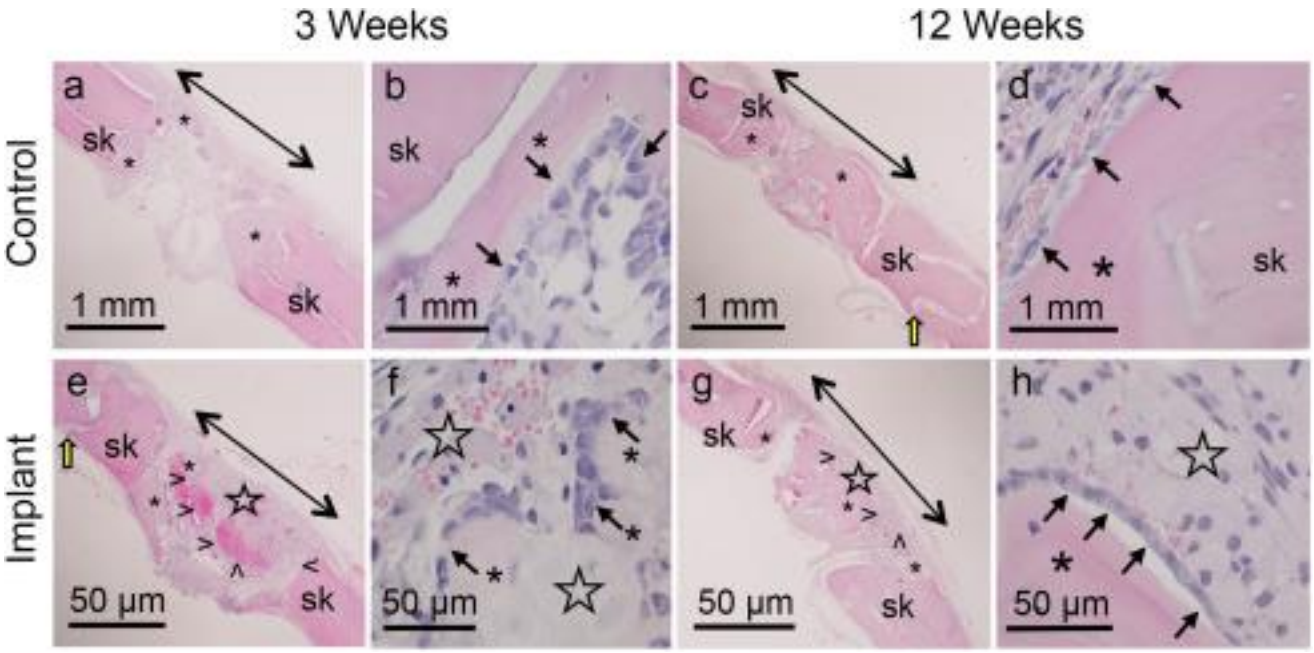

Fig. 7. Histology images taken at (a, b) 3 week control, (c, d) 12 week control, (e, f) 3 week implant, and (g, h) 12 week implant. Images a, c, e, and g indicate the width of the skull defect, given by the double-headed arrows. New bone formation on the defect walls can be seen for all images indicated by the asterisks (*). In addition, images e and g show new bone growth formation throughout the center of the defect on the CNC aerogel (indicated by the star). Yellow arrows in images e and c shows the natural bone suture between adjoining bone plates in the midline of the dorsal skull. Osteogenic activity is evidenced by hypertrophy and hyperplasia of osteoblasts that is noticeably greater at 3 weeks time points (b, f) than at 12 weeks time points (d, h). Osteoblasts can be seen forming a continuous row, forming new bone, on the skull defect walls (indicated by the short arrows), and can be seen forming small areas of bone independently from the bone defect wall in images f and h. sk = skull. (For interpretation of the references to colour in this figure legend, the reader is referred to the web version of this article.)

At 12 weeks post-surgery, the amount of new bone directly in contact with the edges of the skull was increased in control rats (Fig. 7c) and the rows of osteoblasts on its surface still appeared moderately hypertrophied (Fig. 7d). In S-CNC aerogel implanted rats, the amount of bone formation at the edges of the skull and within the scaffolding material was also increased (Fig. 7g). This effect can be associated with more moderate osteoblast hypertrophy (Fig. 7h) and aerogel degradation (Fig. 7g).

Segmentation was performed on reconstructed mCT 3D volumes to calculate bone volume fraction (Table 3). Both the 3 week and 12 week implantation demonstrated significantly higher bone volume fractions than controls with a 33% and 50% increase in BV/TV for 3 and 12 weeks, respectively. Furthermore, both the 3 week and 12 week S-CNC implanted rats showed con tact and distance osteogenesis, marked by bone formation from the center of the bone defect and walls, in contrast to the 3 week and 12 week control that only show bone growth from the bone defect wall (Fig. 8). These results are in accordance with the results shown in (Fig. 7).

Table 3. Bone volume fraction as measured from µCT reconstructions.

***In vivo* sample**	**Bone volume fraction (%)**
3 week Control, n = 5	30 ± 7

12 week Control, n = 5	40 ± 8
3 week S-CNC Implant, n = 4	40 ± 2
12 week S-CNC Implant, n = 4	60 ± 4

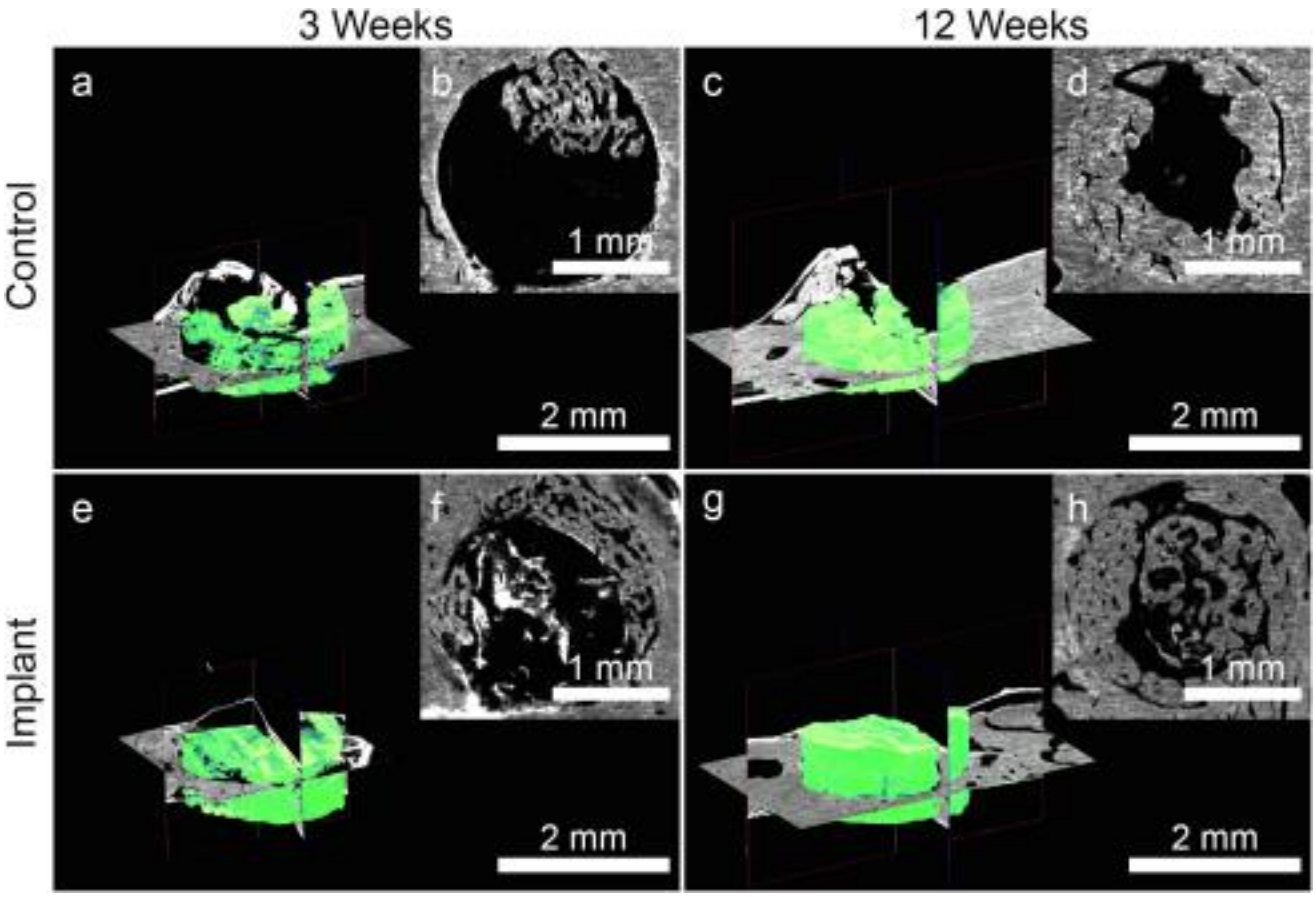

Fig. 8. 3D reconstructions (in green) and orthogonal slices from ICT of 3 week and 12 week time points of the (a, b and c, d) sham control and (e, f and g, h) S-CNC implanted scaffolds. Insets b, d, f, and h are transverse slices through the entire defect site, roughly half way through the cranial bone. S-CNC scaffolds conducted bone throughout the entire defect volume, while control sham sites show bone regeneration only surrounding the defect cavity. (For interpretation of the references to colour in this figure legend, the reader is referred to the web version of this article.)

4. Discussion

Both S-CNC and P-CNC aerogels have been shown here to possess favorable characteristics of a bone scaffold. Their sponge-like properties provide them with the potential advantage of completely filling bone defects [6]. This, coupled with its bimodal pore on average, and the average mesopore size is 6 nm and 11 nm for S-CNC and P-CNC aerogels, respectively, showing that CNC aerogels have a high potential for promoting bone in-growth [46] and cell proliferation [47], along with providing a large surface area to promote cell adhesion. This pore morphology and high porosity also allows the aerogels to efficiently completely fill with the liquid environment they are placed in (without collapsing), which is helpful for in vitro and in vivo testing.

S-CNC aerogels have higher compressive strength at 90% compression than P-CNC aerogels in both dry and wet conditions. This is attributed to P-CNCs having fewer cross-links (according to XPS results in Table 2), potentially due to P-CNCs being slightly aggregated in suspension (primarily CHO-P-CNCs, Table 1). P-CNC aerogel sheets likely consist of regions of aggregated CHO-P-CNCs that are only held together with hydrogen bonds, which are less stable

in aqueous conditions than hydrazone cross-links. Scaffolds with stiffer mechanical properties are preferred for bone tissue growth [48,49]. Therefore, S-CNC aerogels have an advantage over P-CNC aerogels as a bone tissue scaffold with regards to mechanical properties. It should be noted that as the compressive strength of both S-CNC and P-CNC aerogels is far lower than the that of bone [50], these scaffolds should not be used in highly load-bearing applications. Instead, CNC aerogels offer the advantage of being a flexible and expandable scaffold that is capable of form-filling complex bone defects to facilitate bone regeneration. Both S-CNC and P-CNC aerogels were shown to be viable bone cell scaffolds through in vitro tests (Fig. 4). This also shows how the CNC sheets provide a non-cytotoxic environment for cells to remain viable, as cell metabolism was constant between 3 and 7 days for S-CNC aerogels. P-CNC aerogels show a similar trend, as S-CNC and P-CNC aerogel cell metabolism readings were statistically equal at 7 days. However, it should be noted that P-CNC aerogels took longer to become confluent as indicated by the cell metabolism reading at 3 days. This may be due to P-CNC aerogel sheets not being as stiff as S-CNC aerogel sheets, since it has been shown that Saos-2 cells favour stiffer environments [51]. ALP activity was shown to be favourable for both S-CNC and P
CNC aerogels and was statistically equal at 1 and 3 days, but is significantly different at 7 days, where P-CNCs were preferable (Fig. 4d). This is potentially due to the weaker mechanical properties of P-CNC aerogels. For example, at 7 days, P-CNC aerogels began to break down in the media. Therefore, as the lysis solution was added to P-CNC aerogels in media, more cells could be lysed, and therefore a stronger ALP activity was detected. Since S-CNC aerogels stayed intact due to their highly cross-linked structure, the lysis solution could not penetrate into the aerogel to the same extent as in the P-CNCs. It can be argued that the P-CNC aerogels represent the ALP activity of Saos-2 cells more accurately when compared to S-CNC aerogels, due to their increased decomposition morphology, which allows for an influx of osteogenic cells through macropores and better cell adhesion on mesopores, provides unique properties for bone scaffolding. In addition, the inherent non-toxicity of CNCs [45] has allowed for CNC aerogels to facilitate osteogenic cell growth and differentiation, while the anionic groups on CNC surfaces have provided viable nucleation sites for HA.

S-CNC and P-CNC aerogels are similar in their pore morphology, average mesopore size, and specific surface area. The macropores shown in Fig. 1 for both types of aerogels are larger than 100 mm after the 7 days. The expression of ALP from both types of CNC aerogels is a promising result for their use as bone tissue scaffolds. Higher ALP readings generally correspond to increased osteoblast cell differentiation [52,53] and bone mineralization [54] during osteogenesis.

Due to the different degradation properties between S-CNC and P-CNC aerogels in liquids (over the 7 day period tested), there is potential to tune their bioresorbability in an in vivo environment. It has already been shown that the degradation rate of hydrazone cross-linked gels can be controlled with the amount of hydrazone bonds present [23]. Therefore, by tuning the amount of aldehyde and hydrazide content on CNC surfaces, or limiting the amount of hydrazone bonds that can be formed, the degradation rate of CNC aerogels can be tuned.

HA growth occurred on both S-CNC and P-CNC aerogel surfaces that had been pre-treated with 0.1 M $CaCl_2$. This was expected for P-CNC aerogels as many studies have shown that the phosphorylation of cellulose substrates can facilitate HA growth [15–17]. However, S-CNC aerogels show similar HA growth after both 7 and 14 days despite not having any phosphate groups. This was attributed to sulfate half-ester groups ionically binding to calcium ions [55] during the $CaCl_2$ pre-treatment. These calcium ions ionically bind to phosphate ions in the SBF solution so HA can form [56]. Therefore, this work indicates that the phosphorylation of cellulose substrates is not essential for HA growth in SBF, rather the anionic species on the surface impacts HA growth, as has been similarly reported by Rhee and Tanaka on chondroitin sulfate substrates [55]. Though previous work has shown SBF submersion tests are not a guarantee of HA growth in in vivo environments [57], many studies have used SBF to produce HA coatings on scaffold surfaces [16,21,58,59]. Therefore, even if CNC aerogels cannot grow HA naturally in in vivo environments, this procedure can still be used to coat CNC aerogels with HA to further promote cell adhesion, cell proliferation [60], and cell differentiation [61].

In this work, a cavarial defect rodent model was used for studying the effect of CNC aerogels on osteogenesis in bone. Histological analyses of bone to identify regions of mineralization and osteoblasts can be carried out with a wide range of stains, such as, Toluidine Blue, Von Kossa's, Masson's Trichrome, Alcian Blue, or Hematoxylin and Eosin (H and E) which enables visualization of new bone growth, osteoblasts and signs of inflammation [62].

Whereas tartrate resistant acid phosphatase (TRAP) can be used to specifically target osteoclasts during remodelling events [63]. However, studies have shown that an arbitrarily selected histo logical slice can result in misleading conclusions about bone graft materials [64]. Moreover, histology is a time intensive destructive technique that requires chemical modification, including in many cases, decalcification of the bone itself [65]. The advantages of using mCT as a histological alternative have been widely demonstrated in the literature as a non-destructive technique that provides 3D accuracy for the evaluation of osseointegration [66–68]. When compared to histology, it has been shown that mCT shows comparable accuracy when calculating bone volume fraction as histomorphometry from many slices [69]. Moreover, exciting new multi-modal analyses that combine histology and mCT through co-registration of datasets have recently been reported to highlight the degradation and bone regenerative capabilities of b-tricalcium phosphate [70]. A combined characterization approach including mCT and histology is still considered best [65]. Here, mCT has been utilized for its superior 3D visualization of bone and reliable calculation of bone volume fraction. These observations have been supported by H&E staining of histological slices, which confirms new bone growth by osteoblasts, and rules

out signs of severe inflammation.

The in vivo experiments support the findings of in vitro tests; the CNC aerogels are capable of facilitating bone growth within living tissue. Histological analyses and bone volume fraction measurements from mCT clearly show that the CNC aerogel has acted as a scaffold for bone formation, suggesting it is indeed an osteo conductive material. At both time points, S-CNC aerogels regenerated an increased amount of bone compared to controls, 33% more at 3 weeks and 50% more at 12 weeks, as shown in Table 3. As depicted in (Fig. 7), S-CNC implants have bone growth at the defect walls, and some throughout the center of the defect site which likely represent bone growing from the aerogel sheets, which further supports in vitro results that showed that osteogenic cells were able to adhere to S-CNC aerogels surfaces (Fig. 4). These islands of newly formed bone are shown in Fig. 8f and h, as large sections of bone can be seen growing across the bone defect either connecting to or attempting to connect to bone growth on the defect walls. This is in contrast to controls (Fig. 8b and d), where relatively no bone is growing in the center of defect site. Fig. 7 also reveals potential inflammatory cells existing around the islands of bone. This is due to CNC aerogel sheets susceptibility to hydrolytic degradation. When osteoclasts resorb bone they release an acidic environment to break down collagen and hydroxyapatite [71] which could also degrade the hydrazone bonds [18] in the CNC aerogel. It is possible that these components of the degraded aero gel could be targeted by the immune system, which would explain the presence of the inflammatory cells. However, as these studies are at early time points, the presence of these cells is not abnormal in the sequence of de novo bone formation. It should be noted that the identity of the cells internalizing the scaffold remains undetermined but could be analyzed through further histological analyses

5. Conclusion

This work has demonstrated the feasibility of using S-CNC and P-CNC aerogels as bone scaffolds. S-CNC and P-CNC aerogels exhibited ideal scaffold characteristics, including macropores in the range of 10–950 mm to allow cell migration, unique mesopore morphology, and a large specific surface area to promote cell adhesion and proliferation. Both types of aerogels showed an increase in cell metabolism over a 7 day period. ALP activity on both types of aerogels increased with time indicating a healthy environment for cell differentiation. P-CNC aerogels were found to partially break down at 7 days in the cell assays, indicating that by controlling the amount of hydrazone cross-linking between CNCs we can tune the aerogel bioresorbability. SBF testing showed that aerogels were capable of growing HA after a $CaCl_2$ pre-treatment, showing potential for osteoconduction in vivo. S-CNC aerogels also nucleated HA from the sulfate half-ester groups, with the use of a $CaCl_2$ pre-treatment, despite the absence of phosphate groups. S-CNC aero gels generated a bone volume fraction 33% and 50% larger than controls during 3 and 12 weeks, respectively, during in vivo studies in rats. Both histology and mCT 3D reconstructions reveal that aerogel sheets exhibited osteoconductive properties, and promoted the formation of bone across the defect site. In future work, understanding the degradation rate of these scaffolds in vivo and the corresponding cellular activity that drives degradation and remodelling in the implant space is a priority. Longer-term and time-resolved studies that incorporate histological analysis for a wider range of cell types, as well as high resolution studies of the CNC-bone interface, are needed to better quantify the rate of resorption of these scaffolds in vivo. This first in vivo study, and thorough characterization, of chemically cross-linked CNC aerogels has proven their potential as a resorbable osteoconductive bone tissue scaffold in non-load-bearing applications.

Acknowledgments

This work was supported by funding to KG and EC from the Natural Sciences and Engineering Research Council of Canada (NSERC) Discovery Grant Program, grants RGPIN 402329 and RGPIN 588778. The authors would like to acknowledge the assistance of Professors T. Hoare, R. Pelton, A. Gurane, and facilities such as the McMaster Automotive Resource Center (MARC), McMaster Biointerfaces Institute, the Central Animal Facility (CAF) of McMaster University and the University of Waterloo for shared equipment. Electron microscopy was performed at the Canadian Centre for Electron Microscopy, a facility supported by NSERC and other governmental sources. The authors thank, O. Vander fleet, A. Kacheff, J. Tedesco, M. Reid, M. LaGars, V. Jarvis, Dr. D. Cov elli, S. Akmal, G. Hamm, and T. Mihaljevic for training, sample analysis, and expertise. D.A. Osorio would also like to extend a special thanks to X. Yang for his pioneering work on cross-linked CNC aerogels and guidance throughout this work.

Conflict of interest

The authors of this work declare no conflicts of interest.

Appendix A. Supplementary data

Supplementary data to this article can be found online at https://doi.org/10.1016/j.actbio.2019.01.049.

References

[1] S. Bose, M. Roy, A. Bandyopadhyay, Recent advances in bone tissue engineering scaffolds, Trends Biotechnol. 30 (10) (2012) 546–554.
[2] F.J. O'Brien, Biomaterials & scaffolds every day thousands of surgical procedures are performed to replace, Mater. Today 14 (3) (2011) 88–95. [3] S. Preethi Soundarya, A. Haritha Menon, S. Viji Chandran, N. Selvamurugan, Bone, tissue engineering: Scaffold preparation using chitosan and other biomaterials with different design and fabrication techniques", Int. J. Biol. Macromol. 119 (2018) 1228–1239.
[4] C.M. Murphy, M.G. Haugh, F.J. O'Brien, The effect of mean pore size on cell attachment, proliferation and migration in collagen – glycosaminoglycan scaffolds for bone tissue engineering, Biomaterials 31 (3) (2010) 461–466.
[5] K. Tuzlakoglu, N. Bolgen, A.J. Salgado, M.E. Gomes, Nano- and micro-fiber combined scaffolds: a new architecture for bone tissue engineering, J. Mater. Sci. Mater. Med. 16 (12) (2005) 1099–1104.
[6] I. Asahina, M. Watanabe, N. Sakurai, M. Mori, S. Enomoto, Repair of bone defect in primate mandible using a bone morphogenetic protein (BMP)- hydroxyapatite-collagen composite, J. Med. Dent. Sci. 44 (1997) 63–70.
[7] A. Oryan, S. Alidadi, A. Moshiri, Current concerns regarding healing of bone defects, Hard Tissue 2 (2) (2013) 1–12.
[8] Y. Habibi, L.A. Lucia, O.J. Rojas, Cellulose nanocrystals: chemistry, self assembly, and applications, Chem. Rev. 110 (6) (2010) 3479–3500. [9] J.K. Jackson, K. Letchford, B.Z. Wasserman, L. Ye, W.Y. Hamad, H.M. Burt, The use of nanocrystalline cellulose for the binding and controlled release of drugs, Int. J. Nanomedicine 6 (2011) 321–330.
[10] E. Lam, K.B. Male, J.H. Chong, A.C.W. Leung, J.H.T. Luong, Applications of functionalized and nanoparticle-modified nanocrystalline cellulose, Trends Biotechnol. 30 (5) (2012) 283–290.
[11] N. Lin, A. Dufresne, Nanocellulose in biomedicine: current status and future prospect, Eur. Polym. J. 59 (2014) 302–325.
[12] C. Zhou, Q. Shi, W. Guo, L. Terrell, A.T. Quereshi, D.J. Hayes, Q. Wu, Electrospun bio-nanocomposite scaffolds for bone tissue engineering by cellulose nanocrystals reinforcing maleic anhydride grafted PLA, ACS Appl. Mater. Interfaces 5 (9) (2013) 3847–3854.
[13] S. Camarero-Espinosa, B. Rothen-Rutishauser, C. Weder, E.J. Foster, Directed cell growth in multi-zonal scaffolds for cartilage tissue engineering, Biomaterials 74 (2015) 42–52.
[14] S. Camarero Espinosa, T. Kuhnt, E.J. Foster, C. Weder, Isolation of thermally stable cellulose nanocrystals by phosphoric acid hydrolysis, Biomacromolecules 14 (4) (2013) 1223–1230.
[15] K.A. Zimmermann, J.M. Leblanc, K.T. Sheets, R.W. Fox, P. Gatenholm, Biomimetic design of a bacterial cellulose/hydroxyapatite nanocomposite for bone healing applications, Mater. Sci. Eng. C 31 (1) (2011) 43–49.
[16] Y.Z. Wan, Y. Huang, C.D. Yuan, S. Raman, Y. Zhu, H.J. Jiang, F. He, C. Gao, Biomimetic synthesis of hydroxyapatite/bacterial cellulose nanocomposites for biomedical applications, Mater. Sci. Eng. C 27 (4) (2007) 855–864.
[17] K. Yamaguchi, M. Prabakaran, M. Ke, X. Gang, I.M. Chung, I.C. Un, M. Gopiraman, I.S. Kim, Highly dispersed nanoscale hydroxyapatite on cellulose nanofibers for bone regeneration, Mater. Lett. 168 (2016) 56–61.
[18] X. Yang, E. Bakaic, T. Hoare, E.D. Cranston, Injectable polysaccharide hydrogels reinforced with cellulose nanocrystals: morphology, rheology, degradation, and cytotoxicity, Biomacromolecules 14 (12) (2013) 4447–4455.
[19] S. Beck, J. Bouchard, R. Berry, Dispersibility in water of dried nanocrystalline cellulose, Biomacromolecules 13 (5) (2012) 1486–1494.
[20] M.A. Hubbe, O.J. Rojas, L.A. Lucia, M. Sain, Cellulosic nanocomposites: a review, BioResources 3 (3) (2008) 929–980.
[21] C. Huang, N. Hao, S. Bhagia, M. Li, X. Meng, Y. Pu, Q. Yong, A.J. Ragauskas, Porous artificial bone scaffold synthesized from a facile in situ hydroxyapatite coating and crosslinking reaction of crystalline nanocellulose, Materialia (2018).
[22] X. Yang, E.D. Cranston, Chemically cross-linked cellulose nanocrystal aerogels with shape recovery and superabsorbent properties, Chem. Mater. 26 (20) (2014) 6016–6025.
[23] N.M.B. Smeets, E. Bakaic, M. Patenaude, T. Hoare, Injectable and tunable poly (ethylene glycol) analogue hydrogels based on poly(oligoethylene glycol methacrylate), Chem. Commun. 50 (25) (2014) 3306–3309.
[24] H. Zhu, X. Yang, E.D. Cranston, S. Zhu, Flexible and porous nanocellulose aerogels with high loadings of metal – organic-framework particles for separations applications, Adv. Mater. 28 (35) (2016) 7652–7657.
[25] X. Yang, K. Shi, I. Zhitomirsky, E.D. Cranston, Cellulose nanocrystal aerogels as universal 3D lightweight substrates for supercapacitor materials, Adv. Mater. 27 (40) (2015) 6104–6109.
[26] S. Beck-Candanedo, M. Roman, D.G. Gray, Effect of reaction conditions on the properties and behavior of wood cellulose nanocrystal suspensions, Biomacromolecules 6 (2) (2005) 1048–1054.
[27] O.M. Vanderfleet, D.A. Osorio, E.D. Cranston, Optimization of cellulose nanocrystal length and surface charge density through phosphoric acid hydrolysis, Philos. Trans. A 376 (2112) (2017) 20170041.
[28] S. Beck, M. Méthot, J. Bouchard, General procedure for determining cellulose nanocrystal sulfate half-ester content by conductometric titration, Cellulose 22 (1) (2015) 101–116.
[29] S.B. Campbell, M. Patenaude, T. Hoare, Injectable superparamagnets: highly elastic and degradable poly(N-isopropylacrylamide)-superparamagnetic iron oxide nanoparticle (SPION) composite hydrogels, Biomacromolecules 14 (3) (2013) 644–653.
[30] C. Fraschini, G. Chauve, J. Bouchard, TEMPO-mediated surface oxidation of cellulose nanocrystals (CNCs), Cellulose (2017) 1–16.
[31] A.P. Briggs, A colorimetric method for the determination of homogentisic acid in urine, J. Biol. Chem. 51 (2) (1922) 453–454.
[32] S. Bhattacharjee, Review article DLS and zeta potential – What they are and what they are not?, J Control. Release

235 (2016) 337–351.
[33] M.S. Reid, M. Villalobos, E.D. Cranston, Benchmarking cellulose nanocrystals: from the laboratory to industrial production, Langmuir 33 (7) (2017) 1583– 1598.
[34] P.I. Ravikovitch, A.V. Neimark, Characterization of micro- and mesoporosity in SBA-15 materials from adsorption data by the NLDFT method, J. Phys. Chem. B 105 (29) (2001) 6817–6823.
[35] A.M. Seligman, H.L. Wasserhrug, J.S. Hanker, A new staining method (OTO) for enhancing contrast of lipid droplets in osmium-tetroxide fixed tissue osmiophilic thiocarbohydrazide (TCH), J. Cell Biol. 30 (2) (1966) 424–432.
[36] N. Reznikov, R. Shahar, S. Weiner, Three-dimensional structure of human lamellar bone: the presence of two different materials and new insights into the hierarchical organization, Bone 59 (2014) 93–104.
[37] W.J. Lyons, Crystal density of native cellulose, J. Chem. Phys. 9 (4) (1941) 377– 378.
[38] P. De Wolff, ICDD Grant-in-Aid, 1966.
[39] M. Chau, K.J. De France, B. Kopera, V.R. Machado, S. Rosenfeldt, L. Reyes, K.J.W. Chan, S. Fo, E.D. Cranston, T. Hoare, E. Kumacheva, Composite hydrogels with tunable anisotropic morphologies and mechanical properties, Chem. Mater. 28 (10) (2016) 3406–3415.
[40] B.E.J. Lee, H. Exir, A. Weck, K. Grandfield, Characterization and evaluation of femtosecond laser-induced sub-micron periodic structures generated on titanium to improve osseointegration of implants, Appl. Surf. Sci. 441 (2018) 1034–1042.
[41] T. Kokubo, H. Takadama, How useful is SBF in predicting in vivo bone bioactivity?, Biomaterials 27 (15) (2006) 2907–2915
[42] T.T. Nge, J. Sugiyama, Surface functional group dependent apatite formation on bacterial cellulose microfibrils network in a simulated body fluid, J. Biomed. Mater. Res. Part A 81 (1) (2007) 124–134.
[43] F. Cherhal, F. Cousin, I. Capron, Influence of charge density and ionic strength on the aggregation process of cellulose nanocrystals in aqueous suspension, as revealed by small-angle neutron scattering, Langmuir 31 (20) (2015) 5596– 5602.
[44] M. Kalbacova, B. Rezek, V. Baresova, C. Wolf-brandstetter, A. Kromka, Nanoscale topography of nanocrystalline diamonds promotes differentiation of osteoblasts, Acta Biomater. 5 (8) (2009) 3076–3085.
[45] M. Roman, Toxicity of cellulose nanocrystals: a review, Ind. Biotechnol. 11 (1) (2015) 25–33.
[46] M. Zaborowska, A. Bodin, H. Bäckdahl, J. Popp, A. Goldstein, P. Gatenholm, Microporous bacterial cellulose as a potential scaffold for bone regeneration, Acta Biomater. 6 (7) (2010) 2540–2547.
[47] J.E. Davies, Understanding peri-implant endosseous healing, J. Dent. Educ. 67 (8) (2003) 932–949.
[48] D.W. Hutmacher, Scaffolds in tissue engineering bone and cartilage, Biomaterials 21 (24) (2000) 2529–2543.
[49] J.R. Woodard, A.J. Hilldore, S.K. Lan, C.J. Park, A.W. Morgan, J.C. Eurell, S.G. Clark, M.B. Wheeler, R.D. Jamison, A.J.W. Johnson, The mechanical properties and osteoconductivity of hydroxyapatite bone scaffolds with multi-scale porosity, Biomaterials 28 (1) (2017) 45–54
[50] S. Pal, Design of artificial human joints & organs, vol. 9781461462, 2014. [51] K. Anselme, L. Ploux, A. Ponche, Cell/material interfaces: influence of surface chemistry and surface topography on cell adhesion, J. Adhes. Sci. Technol. 24 (5) (2010) 831–852.
[52] M.R. Forwood, M.B. Bennett, A.R. Blowers, R.L. Nadorfi, Modification of the in vivo four-point loading model for studying mechanically induced bone adaptation, Bone 23 (3) (1998) 307–310.
[53] J.E. Aubin, F. Liu, L. Malaval, A.K. Gupta, Osteoblast and chondroblast differentiation, Bone 17 (2) (1995) S77–S83.
[54] E.E. Golub, K. Boesze-Battaglia, The role of alkaline phosphatase in mineralization, Curr. Opin. Orthop. 18 (5) (2007) 444–448.
[55] S.H. Rhee, J. Tanaka, Self-assembly phenomenon of hydroxyapatite nanocrystals on chondroitin sulfate, J. Mater. Sci. Mater. Med. 13 (6) (2002) 597–600.
[56] C.Y. Kim, A.E. Clark, L.L. Hench, Early stages of calcium-phosphate layer formation in bioglasses, J. Non. Cryst. Solids 113 (2–3) (1989) 195–202. [57] A. Cüneyt Tas, Synthesis of biomimetic Ca-hydroxyapatite powders at 37 C in synthetic body fluids, Biomaterials 21 (14) (2000) 1429–1438. [58] Y.W. Gu, K.A. Khor, P. Cheang, In vitro studies of plasma-sprayed hydroxyapatite/Ti-6Al-4V composite coatings in simulated body fluid (SBF), Biomaterials 24 (9) (2003) 1603–1611.
[59] J. Weng, Q. Liu, J.G.C. Wolke, X. Zhang, K. De Groot, Formation and characteristics of the apatite layer on plasma-sprayed hydroxyapatite coatings in simulated body fluid, Biomaterials 18 (15) (1997) 1027–1035.
[60] D.D. Deligianni, N.D. Katsala, P.G. Koutsoukos, Y.F. Missirlis, Effect of surface roughness of hydroxyapatite on human bone marrow cell adhesion, proliferation, differentiation and detachment strength, Biomaterials 22 (1) (2000) 87–96.
[61] R. Budiraharjo, K.G. Neoh, E.T. Kang, Hydroxyapatite-coated carboxymethyl chitosan scaffolds for promoting osteoblast and stem cell differentiation, J. Colloid Interface Sci. 366 (1) (2012) 224–232.
[62] Y.H. An, K.L. Martin, Handbook of Histology Methods for Bone and Cartilage, 2003.
[63] P. Ballanti, S. Minisola, M.T. Pacitti, L. Scarnecchia, R. Rosso, G.F. Mazzuoli, E. Bonucci, Tartrate-resistant acid phosphate activity as osteoclastic marker: sensitivity of cytochemical assessment and serum assay in comparison with standardized osteoclast histomorphometry, Osteoporos. Int. 7 (1) (1997) 39– 43.
[64] A.K. Stalder, B. Ilgenstein, N. Chicherova, H. Deyhle, F. Beckmann, B. Müller, S. Hieber, Combined use of micro computed tomography and histology to evaluate the regenerative capacity of bone grafting materials, Int. J. Mater. Res. 105 (7) (2014) 679–691.
[65] E.L. Hedberg, H.C. Kroese-Deutman, C.K. Shih, J.J. Lemoine, M.A.K. Liebschner, M.J. Miller, A.W. Yasko, R.S. Crowther, D.H. Carney, A.G. Mikos, J.A. Jansen, Methods: a comparative analysis of radiography, microcomputed tomography, and histology for bone tissue engineering, Tissue Eng. 11 (9–10) (2005) 1356– 1367.

[66] F. Peyrin, Evaluation of bone scaffolds by micro-CT, Osteoporos. Int. 22 (6) (2011) 2043–2048.
[67] S.T. Ho, D.W. Hutmacher, A comparison of micro CT with other techniques used in the characterization of scaffolds, Biomaterials 27 (8) (2006) 1362– 1376.
[68] G.H. van Lenthe, H. Hagenmüller, M. Bohner, S.J. Hollister, L. Meinel, R. Müller, Nondestructive micro-computed tomography for biological imaging and quantification of scaffold-bone interaction in vivo, Biomaterials 28 (15) (2007) 2479–2490.
[69] T. He, C. Cao, Z. Xu, G. Li, H. Cao, X. Liu, C. Zhang, Y. Dong, A comparison of micro-CT and histomorphometry for evaluation of osseointegration of PEO coated titanium implants in a rat model, Sci. Rep. 7 (1) (2017) 16270.
[70] A. Sweedy, M. Bohner, G. Baroud, Multimodal analysis of in vivo resorbable CaP bone substitutes by combining histology, SEM, and microcomputed tomography data, J. Biomed. Mater. Res. Part B Appl. Biomater. 106 (4) (2018) 1567–1577.
[71] M.F. Baslé, D. Chappard, F. Grizon, R. Filmon, J. Delecrin, G. Daculsi, A. Rebel, Osteoclastic resorption of Ca-P biomaterials implanted in rabbit bone, Calcif. Tissue Int. 53 (5) (1993) 348–356.